Original Research

Hydroxyapatite Chitosan Gradient Pore Scaffold Activates Oxidative Phosphorylation Pathway to Induce Bone Formation

Zeliang Zhang[1], Wei Shang[2], Lisong Lin[3,*]

[1]Department of Stomatology, The First Affiliated Hospital of Fujian Medical University, 350001 Fuzhou, Fujian, China
[2]Department of Stomatology, The Affiliated Heping Hospital of Changzhi Medical College, 046000 Changzhi, Shanxi, China
[3]Department of Oral and Maxillofacial Surgery, The First Affiliated Hospital of Fujian Medical University, Fujian Provincial Key Laboratory of Stomatology, National Regional Medical Center, Binhai Campus of The First Affiliated Hospital, 350005 Fuzhou, Fujian, China
*Correspondence: dr_lls@163.com (Lisong Lin)
Academic Editor: Francesca Diomede

Abstract

Background: In this study, we prepared a porous gradient scaffold with hydroxyapatite microtubules (HAMT) and chitosan (CHS) and investigated osteogenesis induced by these scaffolds. **Methods**: The arrangement of wax balls in the mold can control the size and distribution of the pores of the scaffold, and form an interconnected gradient pore structure. The scaffolds were systematically evaluated *in vitro* and *in vivo* for biocompatibility, biological activity, and regulatory mechanisms. **Results**: The porosity of the four scaffolds was more than 80%. The 50% and 70% HAMT-CHS scaffolds formed an excellent gradient pore structure, with interconnected pores. Furthermore, the 70% HAMT-CHS scaffold showed better anti-compressive deformation ability. *In vitro* experiments indicated that the scaffolds had good biocompatibility, promoted the expression of osteogenesis-related genes and proteins, and activated the oxidative phosphorylation pathway to promote bone regeneration. Eight weeks after implanting the HAMT-CHS scaffold in rat skull defects, new bone formation was observed *in vivo* by micro-computed tomographic (CT) staining. The obtained data were statistically analyzed, and the p-value < 0.05 was statistically significant. **Conclusion**: HAMT-CHS scaffolds can accelerate osteogenesis in bone defects, potentially through the activation of the oxidative phosphorylation pathway. These results highlight the potential therapeutic application of HAMT-CHS scaffolds.

Keywords: osteogenesis; hydroxyapatite; chitosan; pore scaffold; oxidative phosphorylation

1. Introduction

Bone defects area common orthopedic disease encountered in the clinic. They can cause major damage and require long treatment cycles, thus imposing a heavy medical burden on society [1]. The focus of many researchers has therefore been to identify materials that act as the ideal substitute for bone tissue. Autogenous bone transplantation is still unable to treat diseases related to bone defects. In recent years, bone tissue engineering has been promising approach for production of the best bone tissue replacement materials in recent years [2]. In addition to hydroxyapatite (HAP), other novel materials such as graphene, electrospinning, hydrogels and chitin, have been reported. HAP has the molecular formula $Ca_{10}(PO_4)_6OH_2$, a theoretical Ca/P molar ratio of 1.67, and a hexagonal crystal system. The mineral in bone is carbonate apatite, which is calcium-poor (Ca/P molar ratio <1.67). In addition to calcium and phosphorus, carbonate apatite contains sodium, magnesium and hydrogen phosphate ions, as well as some trace elements. HAP is consistent with the composition of human bone and is considered to be the most closely related material [3]. Its excellent biocompatibility and bioactivity, good bone bonding and bone conduction, and non-toxic side effects, have meant that it occupies a central position in the field of bone repair materials.

Advances in technology, have allowed changes in the microscopic shape of materials, including the production of spherical, rod, and tube shapes as well as the production of nanoscale materials. A review of the literature reveals; that only a few studies [4–9] have been published on tubular materials, mainly on carbon nanotubes and hydroxyapatite microtubules (HAMT). In 1991, Ijima [10] reported on a hollow tube with a nanoscale diameter that was made of curled graphite sheets at a specific spiral angle. The advantages of carbon nanotubes are: (1) They enhance the mechanical properties of tissue engineering materials; (2) They provide or enhance electrical conductivity, thus regulating the cell growth rate and inducing tissue arrangement; (3) They have a high specific surface area, which is conducive to protein adsorption and adhesive cell growth; (4) The structure and appropriate porosity of nanonetworks is conducive to the exchange of materials between cells and the extracellular matrix [10].

Carbon nanotube tissue engineering materials have also become a research hotspot in recent years. Ma *et al*. [4] synthesized a poly-l-lactic acid (PLLA) scaffold with carbon nanotube coating. The original porosity and permeability of the scaffold remained unchanged, but the specific surface area was increased by the coating [4]. The content of carbon nanotubes in the composite material must be

controlled, since a content can form an aggregation structure [11]. Kolos and Ruys [5,6] developed a novel method for the preparation of HAMT using biomimetic coating. Cotton wool was bionic coated by phosphorylation pretreatment and a Ca(OH)$_2$ soaking solution in 5.0 simulated body fluid. The HAMT are formed by sintering and the cotton matrix is then burned [5,6]. Yuan *et al*. [12] used sol-gel auto-combustion method to prepare ordered HAP nanotubes in porous anodic alumina templates. Hui *et al*. [7] prepared fluoro-substituted HAP nanotubes using a hydrothermal method, but the product was in pure due to the presence of fluoride ions. Chandanshive *et al*. [8] synthesized HAP nanotubes with the template method, but the products were polycrystalline and had poor mechanical properties. Ma *et al*. [13] added CaCl$_2$ and NaH$_2$PO$_4$ into the solvent mix of water and N,N-Dimethylformamide for 24 h at 160 °C to prepare HAMT using a one-step method with a relatively simple flow. Zhang *et al*. [9] successfully synthesized HAMT using CaCl$_2$, NaOH, (NaPO$_3$)$_6$, oleic acid, deionized water and ethanol as reaction systems. These HAMT had good biocompatibility, were monodisperse and monocrystalline and had ultra-long life. A tubular structure has good drug loading and slow release properties, and has broad application in the field of medicine and biology [9].

In recent years, nano-HAP has been widely used in biological materials [14]. However, it is difficult to for nano-HAP to meet the requirements as a scaffold for bone tissue engineering due to its low mechanical strength and low toughness [15]. The HAMT prepared in the present study is mechanically stronger than nano-HAP, simple to produce, cost-effective, and also has good biocompatibility [16–18]. We conducted a literature search of papers published over the past 15 years with the key word "hydroxyapatite", "hydroxyapatite microtubules", "chitosan" and "bone tissue engineering". Researchers have paid attention to the material characteristics, as well as to its structure. Porous scaffolds have proven to be a reasonable design, and the pore size, porosity, and arrangement can affect osteogenesis. In the current study, we synthesized a gradient pore scaffold using HAMT and chitosan (CHS) as raw materials, with wax spheres used as the pore forming material. The characterization, biocompatibility, and biological activity of the materials were systematically evaluated. The scaffolds have excellent drug loading and controlled-release ability. Moreover, the design of the gradient pore is similar to the structure of natural bone, and is expected to have good osteogenic effects and therapeutic function in bone defects.

2. Materials and Methods

2.1 Fabrication Process for Scaffolds

2.1.1 Preparation of Hydroxyapatite Microtubules

The preparation method described by *Zhang et al.* [16], was employed here. Ultrapure water (Direct-pure

UPU, Shanghai, China) (4.5 mL), anhydrous ethanol (China National Pharmaceutical Group Corporation, Beijing, China) (8.5 mL), and oleic acid (China National Pharmaceutical Group Corporation, Beijing, China) (7 mL) were stirred for 5 min at room temperature. Next, 10 mL each of CaCl$_2$ (Xilong Chemical, Guangdong, China) (200 mM), NaOH (Xilong Chemical, Guangdong, China) (1.65 M) and (NaPO$_3$)$_6$ (Xilong Chemical, Guangdong, China) (31.45 mM) solutions were added drop by drop to the solution prepared in the first step. A magnetic stirrer provided continuous stirring throughout the procedure. This suspension was then transferred to a reactor and placed in a constant temperature drying oven (JTONE/101-1AB, Shanghai, China) preheated to 180 °C for 25 h. Afterward, the reactor was cooled to room temperature, the final product was washed with anhydrous ethanol and ultra-pure water, centrifuged and dried for use.

2.1.2 Preparation of Wax Balls

Polyvinyl alcohol (PVA) (Xilong Chemical, Guangdong, China) particles (4 g) were added to pure water (200 mL) to prepare a 2 wt% PVA suspension. A heated and melted paraffin (China National Pharmaceutical Group Corporation, Beijing, China) solution (20 mL) was added to the PVA suspension with continuous stirring for 10 minutes. The paraffin-PVA solution was then poured into cold water to terminate the reaction, and the wax balls with a diameter of 500–800 µm and 800–1430 µm were screened.

2.1.3 Preparation of the Scaffolds

The mold was a cylindrical shape with a base diameter of 8 mm and a height of 5 mm. Wax balls (800–1430 µm) were arranged 4 mm around the mold, and 500–800 µm wax balls were arranged in the central 4 mm. Heating at a constant temperature of 37 °C for 30 min can soften the wax balls and induce connections with each other. CHS powder (Aladdin, Shanghai, China) was dissolved in a 1% acetic acid solution (Aladdin, Shanghai, China) to obtain a CHS solution with a concentration of 2 wt%. In the final step, HAMT was added to give as HAMT:CHS mass ratio of 7:3 and stirred continuously at room temperature for 6 h. The mixed slurry was injected into the mold, and freeze-dried (Scientz-12N, Ningbo, China) to obtain a complete scaffold. The scaffold was immersed in n-hexane (Xilong Chemical, Guangdong, China) solution and placed in a water bath at 55 °C. The solution was changed every 1 h, until the wax balls inside the scaffold could be removed. Repeated rinsing with phosphate buffer saline (PBS) removed any residual n-hexane. The 70% HAMT-CHS scaffolds were freeze-dried after cleaning and disinfection. The HAMT:CHS ratio was adjusted to 5:5/9:1. The 50% HAMT-CHS and 90% HAMT-CHS scaffolds, as well as the CHS scaffolds without HAMT were prepared by the same method as the control group.

2.2 Physicochemical Characterization of Scaffolds

Scaffold morphology was observed by scanning electron microscopy (SEM, Zeiss Merlin Compact, Zeiss, Oberkochen, Germany). Fourier transform infrared spectroscopy (FTIR, Nicolet iS20, Thermo Fisher Scientific, Waltham, MA, USA) detects the sent composition in the wave range of 400–4000 cm^{-1}. An X-ray diffractometer (XRD, Rigaku Smartlab 3KW, Tokyo, Japan) was used to determine the composition of the material and the structure of the atoms or molecules inside the material. The scanning angle was 10°–80° and the scanning speed was 2°/min. The porosity of the support was analyzed by a high-performance automatic mercury imposer (Micromeritics AutoPore IV 9520, Atlanta, GA, USA) as described previously [19]. A universal testing machine (Shimadzu AGS-X-50N, Kyoto, Japan) was used to evaluate the mechanical properties of the support and to obtain mechanical indexes such as the compressive strength and elastic modulus. The size of the test sample was φ8 mm $\times$ h5 mm, and the axial loading rate was 1 mm/min until the sample failed. The mechanical properties of the scaffold were analyzed to assess its compressive capacity.

2.3 Measurement of Drug Slow-release

The scaffolds and phenytoin sodium (MCE, Rockville, NJ, USA) PBS solution (100 mg/L) were placed in a shaker at 37 °C for 24 h at 140 r/min. Immediately after drug loading, the freeze-drying processing was carried out for 24 h. The drug-carrying scaffold was added to 10 mL of PBS, and 3 mL of the release solution was removed at a preset time, and an equal volume of PBS was added. Each set of scaffolds contained four samples and were stored in a 37 °C incubator and shaken at 140 r/min for 24 h before each preset time point. Subsequently, the absorbance of the release medium at 258 nm was measured by an ultraviolet spectrophotometer (MAPADA/UV-1200, Shanghai, China).

2.4 Fluorescent Staining

Extract liquor was prepared according to the criteria *ISO*10993-5:2009 and *ISO*10993-12:2012. Rat bone marrow mesenchymal stem cells (BMSCs) were inoculated onto pore plates and cultured for 24 h. The culture medium was then replaced with extract from the corresponding group, and the culture continued for 48 h before staining. The residual serum was rinsed with PBS, diluted 1000 times with Calcein-AM/PI stock solution (Beyotime, Shanghai, China), then added into the well, and incubated at 37 °C for 30 min. Absorbing the staining solution in the hole, the cells were rinsed with PBS several times and observed under the fluorescence of 488 nm wavelength. The cells were gently rinsed with PBS twice, fixed with 4% paraformaldehyde for 15 min, the fixed solution was sucked away, washed with PBS twice, and each well was stained with Phalloidin (Abclonal, Wuhan, China) (1:200 dilution) 250 μL

for 30 min. After absorbing Phalloidin solution, rinsing with PBS twice, adding 250 μL 2-(4-Amidinophenyl)-6-indolecarbamidine dihydrochloride (DAPI) solution (Servicebio, Hubei, China) to each well for 3 min, absorbing the staining solution, washing with PBS twice, fluorescent staining was performed. Result in the observation of cells by fluorescence microscope (IX73, Olympus, Tokyo, Japan). Rat BMSCs were provided by the Shanghai Fusheng Company. All cell lines were maintained at 37 °C in a 5% CO$_2$ atmosphere and were validated by short tandem repeat (STR) profiling and free of mycoplasma (Minerva-Biolabs Mycoplasma Detection Kit, Berlin, Germany). Primary rat BMSCs were cultured for the 3, 4, or 5 passages for subsequent experiments.

2.5 Cell Counting Kit-8 (CCK-8) Experiment

Sterilized scaffolds were placed into a 96-well plate, and 100 μL of medium was added to each well and to soaked for 24 h. The third generation of rat BMSCs were seeded onto the scaffold at 2×10^3 cells/well. Cell viability was evaluated by CCK-8 assay (Beyotime, Shanghai, China) on the 1st, 3rd, 5th and 7th days by using a microplate reader (Infinite M Plex, TECAN, Männedorf, Switzerland) to accurately measure the absorbance at 450 nm (Each set of scaffolds contained four samples).

2.6 Alkaline Phosphatase (ALP) Staining

Rat BMSCs was seeded into 6-well plates for 24 h. The culture medium was then removed with the corresponding extraction solution added. After 7 days, the medium was removed and the cells rinsed with PBS. ALP staining solution (300 μL) (Biosharp, Beijing, China) was then added and incubated at 37 °C for 30 min, followed by three rinsed with PBS before evaluation.

2.7 RT-PCR

After culturing cells for 14 days, PureLink RNA MiniKit (Thermo Fisher Scientific, Waltham, MA, USA) was used to isolate total RNA as recommended by the manufacturer. A NanoDrop-1000 instrument (Thermo Scientific NanoDrop™ 2000/2000c) was used to assess the concentration and quality of RNA. Complementary DNA was obtained and replicated by using the Revert Aid First Strand cDNA Synthesis Kit and the 7500 Fast Real-Time PCR System (StepOnePlus, Applied Biosystems, Carlsbad, CA, USA), respectively. The expression of genes was determined by TaqMan gene expression assays (Applied Biosystems, CA, USA). Relative gene expression was calculated using the $2^{-\Delta\Delta CT}$ method with glyceraldehyde-3-phosphate dehydrogenase (GAPDH) as the control gene, and each set of scaffolds contained four samples. The primer (purchased from Sangon Biotech, Shanghai, China) is detailed in Table 1.

Table 1. The primer sequence table.

Gene	Primer
GAPDH	5′-AAGTTCAACGGCACAGTCAAGG-3′
	5′-GACATACTCAGCACCAGCATCAC-3′
ALP	5′-ACTGATGTGGAATATGAACTGGATGAG-3′
	5′-ATAGTGGGAGTGCTTGTGTCTAGG-3′
BMP	5′-GAACAGGGCTTCCACCGTATAAAC-3′
	5′-TGTCCAGTAGTCGTGTGATGAGG-3′
OCN	5′-CTCTGAGTCTGACAAAGCCTTCATG-3′
	5′-CTCCAAGTCCATTGTTGAGGTAGC-3′
OPN	5′-GACGACGATGACGACGGAGAC-3′
	5′-TGTGTGCTGGCAGTGAAGGAC-3′
OSX	5′-GCTCTTCTGACTGCCTGCCTAG-3′
	5′-TGGTGAGATGCCTGCATGGATG-3′
RUNX2	5′-ACTTCGTCAGCGTCCTATCAGTTC3′
	5′-CCATCAGCGTCAACACCATCATTC-3′

2.8 Western Blot

The cells were cultured with scaffolds for 14 days and then lysed with radio immunoprecipitation assay lysis buffer (Beyotime, Shanghai, China). Isolated proteins were separated and then electro-transferred onto a polyvinylidene difluoride (PVDF) membranes with 0.45 μm pore size. The PVDF membranes were blocked by incubation with 5% BSA (Beyotime, Shanghai, China) at room temperature for 2 h, then incubated with primary antibodies against osteopontin (OPN, dilution 1:100, Abcam ID: ab307994, Cambridge, UK), Osterix (OSX, dilution 1:100, Abcam ID: ab209484, Cambridge, UK), runt-related transcription factor 2 (RUNX2, dilution 1:100, Abcam ID: ab76956, Cambridge, UK), and GAPDH (dilution 1:500, Abclonal ID: AC054, Wuhan, China). After overnight incubation at 4 °C, the membranes were incubated for 1 h at room temperature with a second antibody (horseradish peroxidase (HRP) Goat Anti-Mouse IgG (H+L), dilution 1:500, Abclonal ID: AS003, Wuhan, China; Goat Anti-Rabbit IgG (H+L) HRP, dilution 1:500, Affbiotech ID: S0001, Jiangsu, China) labeled with horseradish peroxidase. An ECL staining kit (Beyotime, Shanghai, China) then was used to detect the protein bands. Gel-pro analyzer 4.0 (Media Cybernetics, Bethesda, MD, USA) analyzed the gray value of each strip, with at least three biological replicates per protein. Graph-Pad Prism 9.1.2 software (GraphPad Software, San Diego, CA, USA) was used for significance analysis.

2.9 RNA Sequencing Technology

The cells were inoculated on the scaffold, cultured for 14 days, and the RNA was then extracted by repeatedly washing the scaffold with Trizol. An Agilent 2100 bioanalyzer (Agilent, Palo Alto, CA, USA) was used to quantify and identify extracted RNA samples to accurately determine the RNA integrity. The messenger RNA (mRNA) of qualified samples was amplified by quantitative real-time polymerase chain reaction (RT-PCR) and purified to obtain the final library. In the second step, initial quantification was performed using a Qubit2.0 fluorometer (Invitrogen, Carlsbad, CA, USA), followed by library insertion size measurements using an Agilent 2100 bioanalyzer. To ensure the quality of the library, the effective concentration (>2 nM) was accurately quantified by quantitative polymerase chain reaction (q-PCR), and clustering and sequencing were subsequently performed. Clean reads were obtained after filtering the raw data, checking the sequencing error rate, and checking the guanine and cytosine content distribution checking. The DESeq2 (1.20.0) R package (https://bioconductor.org/packages/release/bioc /html/DESeq2.html) [20] was used to analyze differential gene expression analysis. The filter criterion was |log2 (FoldChange)| > 1 & p-adj < 0.05. Gene ontology (GO) enrichment of differentially expressed genes and pathway analysis of Kyoto Encyclopedia of Genes and Genomes (KEGG) were performed using the ClusterProfiler R package (https://bioconductor.org/packages).

2.10 Validation of Signaling Pathways

RNA sequencing (RNA-seq) technology helps to identify activated pathways and differentially expressed genes. The protein expression level of key genes and the level of specific oxidases were evaluated to determine which pathways were activated. The key genes are Fe-S protein 5 (NDUFS5, dilution 1:1000, GeneTex ID: GTX101829, San Antonio, TX, USA) and cytochrome c oxidase subunit 6c (COX6C, dilution 1:500, Zenbio ID: R24043, Chengdu, China). Oxidative phosphorylation pathway inhibitor carbonyl cyanide 4-(trifluoromethoxy) phenylhydrazone (FCCP, MCE, NJ, USA). The CCK-8 assay was used to determine the 50% inhibitory concentration of FCCP. The culture medium diluted FCCP to various concentrations and co-cultured with the cells for 3 days. The 50% inhibitory concentration was determined using the CCK-8 assay, and the optimal FCCP concentration for pathway blockade was determined based on the results. The studied pathway was inhibited by FCCP and Western blot experiments were performed to verify whether key genes were down-regulated.

2.11 Animal Experiments

SD male rats (10 rats, 8 weeks old, approximately 270 g, purchased from SPF Biotechnology Co., Ltd., Beijing, China) underwent general anesthesia by intraperitoneal injection of 1% tribromoethanol (Aladdin, China) at 0.02 mL/g body weight. A 3 cm incision was made designed in the middle of the skull to separate the subcutaneous tissue from the bone surface, and an 8 mm trephine was then used to remove part of the skull, taking care not to damage the dura. The scaffolds were placed into the defect and the wound was sutured. After 2 months of conventional environment, the rats were euthanized by excessive carbon dioxide inhalation, and the skull defect was examined
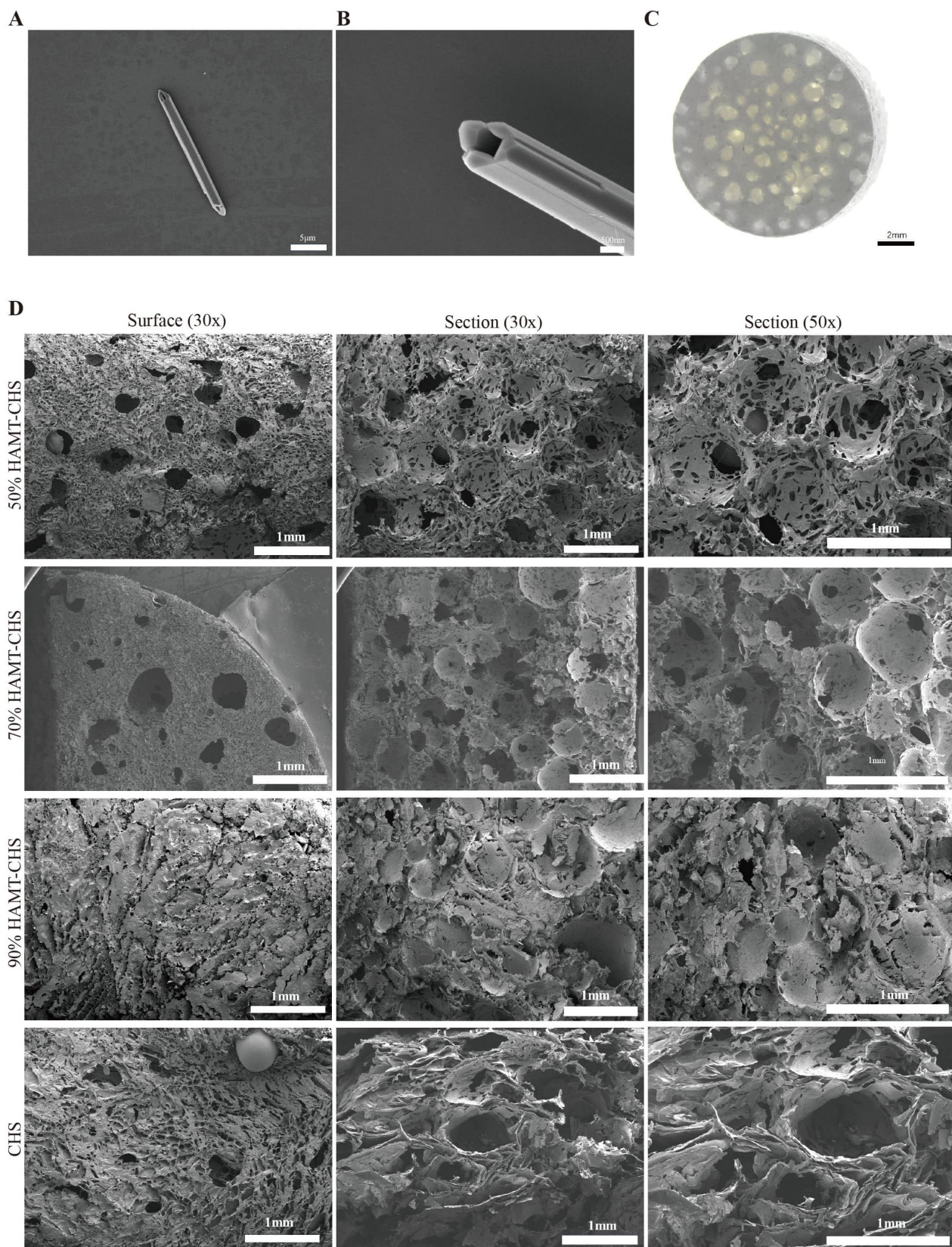
Fig. 1. Characterization of HAMT-CHS scaffolds. (A) The tubular structures of hydroxyapatite microtubule (Scale bar: 5 µm). (B) The same as (A) but for 2×10^4 resolution (Scale bar: 500 nm). (C) The morphology of the scaffold under a stereomicroscope (Scale bar: 2 mm). (D) Surface and section SEM images of HAMT-CHS scaffolds. HAMT, hydroxyapatite microtubules; CHS, chitosan; SEM, scanning electron microscopy (Scale bar: 1 mm).
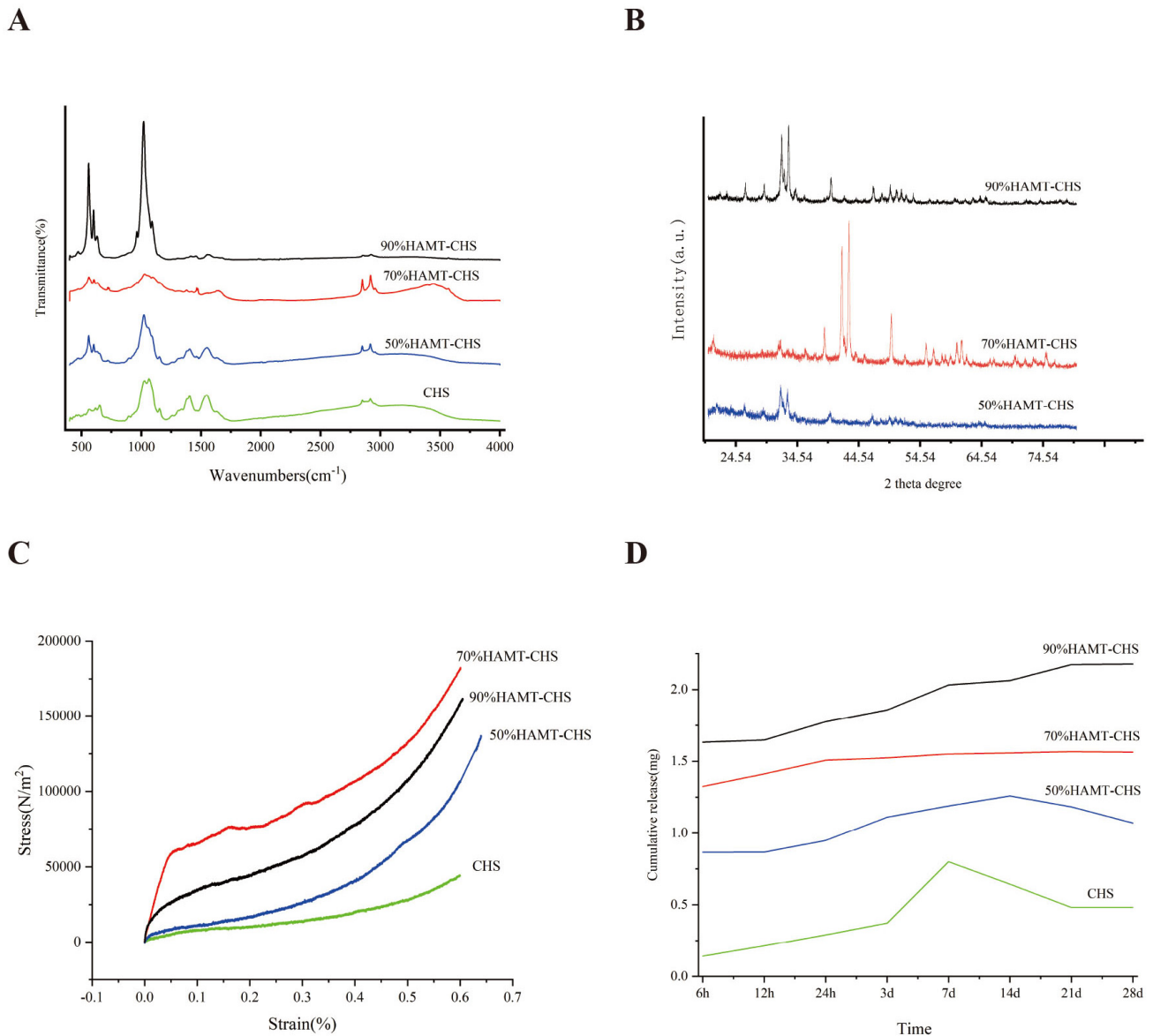
Fig. 2. Physical and drug loading performance of HAMT-CHS scaffolds. (A) The position of the peak of each functional group in the FTIR spectra. (B) The X-ray diffraction results of each group of the scaffolds. (C) Stress-Strain curve. Elastic modulus of the support was CHS (44.383 ± 0.073 MPa), 50% HAMT-CHS (97.548 ± 0.169 MPa), 70% HAMT-CHS (166.717 ± 0.031 MPa), and 90% HAMT-CHS (118.119 ± 0.199 MPa). (D) Cumulative release curve. Sustained drug release was observed in the 90% HAMT-CHS and 70% HAMT-CHS groups within 28 days, and the statistical curve trend showed that the release was more stable in the 70% HAMT-CHS group (Sample size n = 4). FTIR, fourier transform infrared spectroscopy.

by Micro-CT (Skyscan1276, Bruker, Saarbrucken, Germany). The following variables were measured: tissue volume (TV), bone volume (BV), bone surface (BS), trabecular thickness (Tb.Th), trabecular separation (Tb.Sp), and trabecular number (Tb.N), bone volume fraction (BV/TV), bone surface fraction (BS/BV), bone surface area density (BS/TV). The study was carried out in accordance with the revised Animals (Scientific Procedures) Act 1986 in the UK and Directive 2010/63/EU in Europe and approved by the Ethics Committee of Ethics Committee of the Changzhi Medical College (Protocol No. DW2022082).

2.12 Statistical Analysis

Graphpad Prism 9.1.2 (GraphPad Software, San Diego, CA, USA) was used to compare the results of the HAMT-CHS group and the blank group by T-test, with a p-value of <0.05 considered to be significant.

3. Results

3.1 Characterization of HAMT-CHS Scaffold

Tubular structures of the prepared HAP powder were examined by scanning electron microscopy (SEM) under two resolutions (Fig. 1A,B). With a stereomicroscope,

pores of varying size were found on the outer surface of the gradient pore scaffold (Fig. 1C). The four scaffold groups were observed to have a rough surface under SEM, scaffolds prepared solely by CHS did not form a good pore structure on the surface and in cross section (Fig. 1D). However, pore structures on the surface and in cross section were observed for the of 50% HAMT-CHS and 70% HAMT-CHS scaffolds, with cracks penetrating between the pores. The 90% HAMT-CHS scaffold did not show uniform pore structure, either on the surface or in cross section (Fig. 1D).

3.2 Physical and Drug Loading Performance of HAMT-CHS Scaffolds

The position of the peak of each functional group in the FTIR spectra is basically consistent with that of chitosan and hydroxyapatite (Fig. 2A). X-ray diffraction results also showed obvious differences between the three scaffolds (Fig. 2B). The hydroxyapatite materials in the scaffolds were crystallized into standard hydroxyapatite structures, and the diffraction peaks and intensities were consistent with those of standard hydroxyapatite cards. Chitosan is amorphous and hence, no significant peak form was observed. The elastic modulus results for support were as follow: CHS (44.383 ± 0.073 MPa), 50% HAMT-CHS (97.548 ± 0.169 MPa), 70% HAMT-CHS (166.717 ± 0.031 MPa), and 90% HAMT-CHS (118.119 ± 0.199 MPa). The addition of HAMT significantly improved the compressive performance of the scaffold, with the 70% HAMT-CHS scaffold being the best amongst the four groups. When the HAMT material accounted for 90% of the scaffold, the pressure resistance was weaker compared to the 70% scaffold (Fig. 2C).

Plotting the 28-day cumulative release curve showed that the 90% HAMT-CHS scaffold had the highest drug loading capacity, and the CHS scaffold the lowest (Fig. 2D). This result indicates the HAMT material has good drug loading capacity, and that the higher the proportion of HAMT in the scaffold, the greater the drug loading capacity. The CHS group and the 50% HAMT-CHS group showed no significant difference in drug release at 7 and 14 days. The drug concentration was continuously diluted after new PBS solution was added to the samples, and hence the curve showed a downward trend (Fig. 2D). Sustained drug release was observed with the 90% HAMT-CHS and 70% HAMT-CHS scaffolds in the first 28 days, with more stable in the 70% HAMT-CHS group (Fig. 2D). The porosity of the four scaffold groups was: CHS (85.3%), 50% HAMT-CHS (84.1%), 70% HAMT-CHS (88.8%), and 90% HAMT-CHS (80%).

3.3 Biocompatibility of the HAMT-CHS Scaffolds Co-Cultured with BMSCs

Co-culture experiments with BMSCs were performed to assess the biocompatibility of HAMT-CHS scaffolds. Live and Dead Cell Double staining kit (Calcein-AM/PI) and fluorescence staining showed good cell growth in each group, with very few dead cells (Fig. 3A,B). Furthermore, no obvious difference in ALP staining was observed between the four scaffold groups (Fig. 4A). The results of the CCK-8 experiment also showed that no cytotoxicity after co-culture of the scaffolds and BMSCs in any of the four groups. Moreover, the cell proliferation rate was greatly increased, especially in the 50% and 70% HAMT-CHS scaffold groups, but was lower in the CHS group (p-value < 0.05, Fig. 4B). In summary, these results demonstrate that HAMT-CHS scaffolds can promote the growth and proliferation of BMSCs.

3.4 HAMT-CHS Scaffolds Regulate the Expression of Osteogenesis-Associated Genes

To study how HAMT-CHS scaffolds modulate the cellular phenotype of BMSCs, we examined the expression pattern of several essential genes in osteogenesis. Expression level of *OPN*, *RUNX2*, *BPM4*, and *OSX* were significantly higher in 90% HAMT-CHS group than in the other groups (p-value < 0.05, Fig. 5A–D). Significant upregulation of the *RUNX2*, and *BMP4* genes were also observed in the 70% HAMT-CHS group (p-value < 0.05, Fig. 5C,D). Down-regulation of ALP was also observed (p-value < 0.05, Fig. 5E).

Based on the results of fluorescence staining, the CCK-8 assay, ALP staining, RT-PCR, and the mechanical properties of the four scaffold groups, the 70% HAMT-CHS scaffold was selected for subsequent experiments. The results of Western blot analysis showed that higher expression of the OPN, OSX and RUNX2 proteins in the 70% HAMT-CHS group compared to the CHS group (p-value < 0.05, Fig. 5F).

3.5 Exploration of the Signaling Pathways Regulated by HAMT-CHS Scaffolds

To further investigate the underlying mechanisms for the effect of HAMT-CHS scaffolds on the BMSCs phenotype RNA-seq analysis was performed on BMSCs co-cultured with 70% HAMT-CHS or CHS. A total of 4702 differentially expressed genes (DEGs) were identified, including 1862 up-regulated and 2840 down-regulated DEGs (Fig. 6A). GO and KEGG analysis was then performed on all up-regulated DEGs, with the results indicating a significant enrichment of the oxidative phosphorylation pathway (Fig. 6B). *NDUFS5* and *COX6C* are the key genes in this pathway, and their higher expression levels in HAMT-CHS group was verified by Western blot analysis (p-value < 0.01) (Fig. 6C). Nicotinamide-adenine dinucleotide (NAD) and reduced form of nicotinamide-adenine dinucleotide (NADH) are redox pairs, that participate in oxidative phosphorylation [21]. The NADH/NAD ratio in the HAMT-CHS group was 0.824, while in Blank was only 0.09 (Fig. 6D). An increased NADH/NAD ratio indirectly reflects up-regulation of the oxidative phosphorylation process. The CCK-8 assay was used to determine the 50% inhibitory concentration of FCCP. As there was no effect
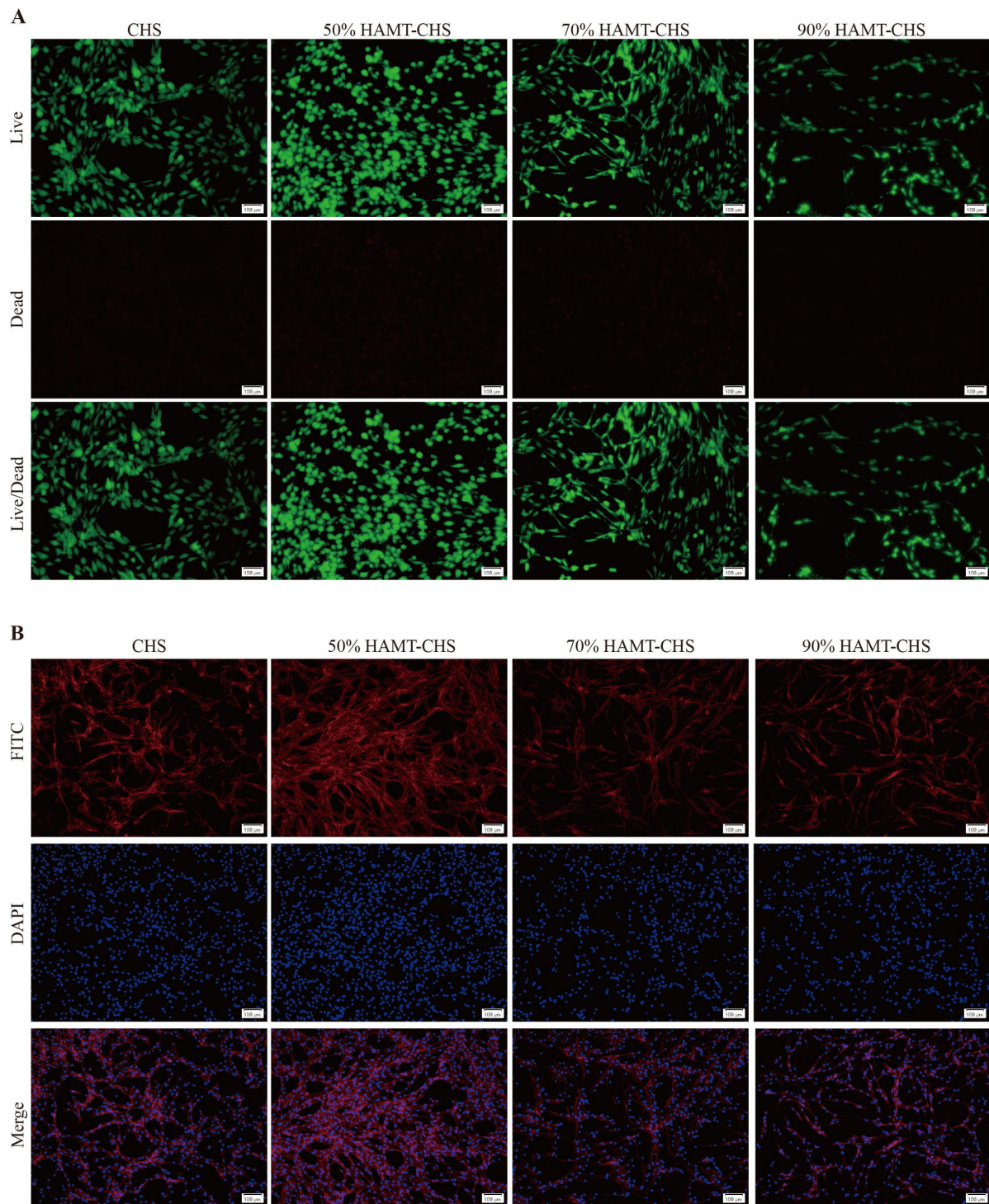
Fig. 3. Biocompatibility test. Calcein-AM/PI Staining (A) (Scale bar: 100 μm), and Fluorescence staining (B) (Scale bar: 100 μm) for BMSCs that were co-cultured with CHS and HAMT-CHS scaffold extracts (Sample size n = 4). BMSCs, bone marrow mesenchymal stem cells; DAPI, 2-(4-Amidinophenyl)-6-indolecarbamidine dihydrochloride; FITC, fluorescein isothiocyanate; Calcein-AM/PI, Live and Dead Cell Double staining kit.

($p > 0.05$) on cell proliferation in the medium with a concentration of 1 μM FCCP compared with the blank group (Fig. 6E), we selected 1 μM concentration of FCCP for following experiment. Following the co-cultured of BMSCs with 1 μM FCCP for 14 days, Western bolting analysis revealed lower expression levels of NDUFS5, COX6C, RUNX2, OPN and OSX compared to the Blank sample (p-value < 0.01) (Fig. 6F). The results suggest the oxidative phosphorylation pathway was inhibited by FCCP, and while the osteogenic effect was weakened.
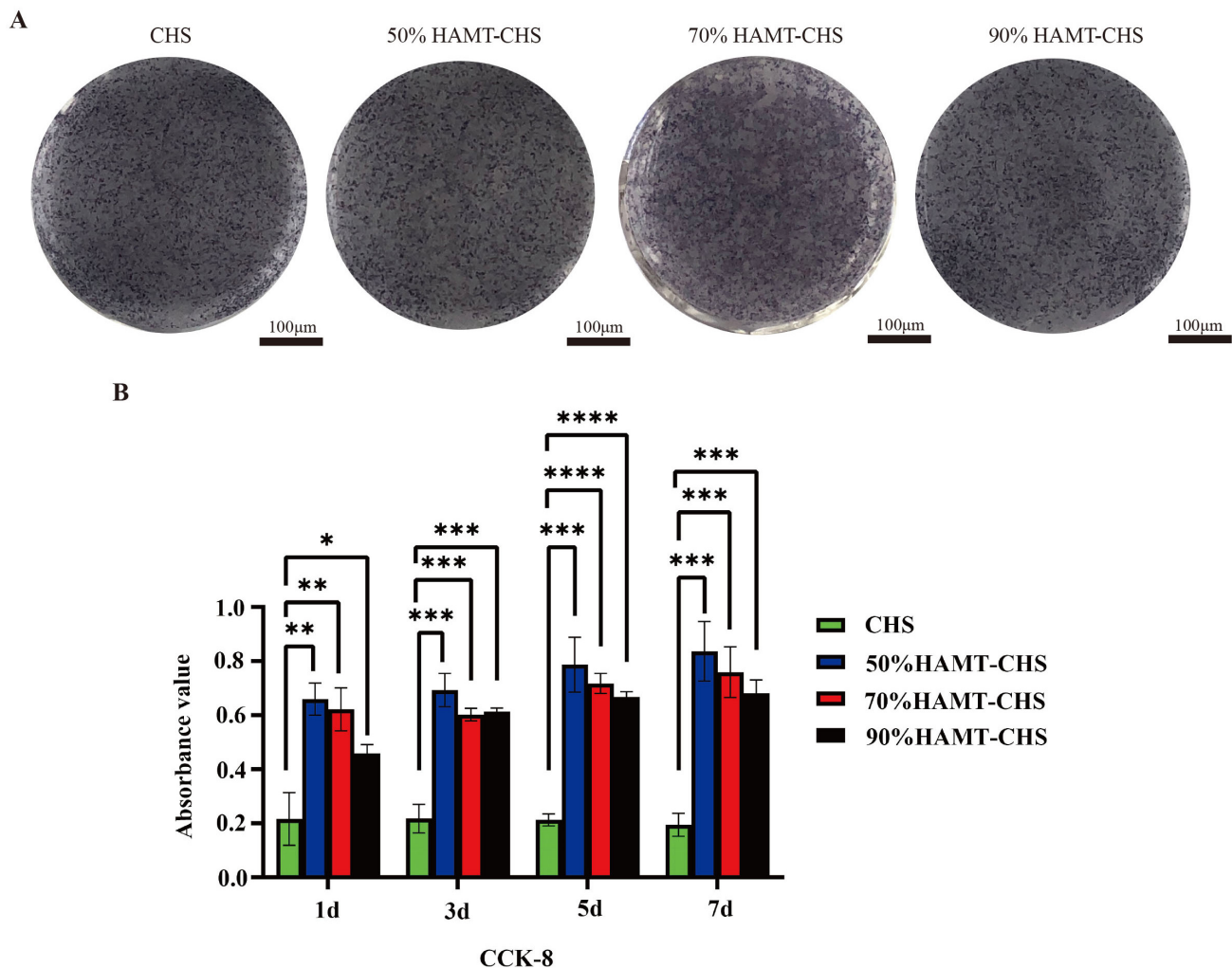
Fig. 4. Biocompatibility of the HAMT-CHS scaffolds co-cultured with BMSCs. (A) The ALP staining result of BMSCs that were co-cultured with scaffold extracts for 7 days (Scale bar: 100 μm). (B) The CCK-8 result of BMSCs that were co-cultured with scaffold extracts for 7 days. "*", "**", "***", "****" represent $p < 0.05$, $p < 0.01$, $p < 0.001$, $p < 0.0001$, respectively (Sample size n = 4). ALP, alkaline phosphatase; CCK-8, Cell Counting Kit-8.

3.6 Animal Experiments Validate the Biocompatibility of HAMT-CHS

To further validate the biological functions of the HAMT-CHS scaffold *in vivo*, we performed the animal experiment described in the (Materials and methods part). Two months after surgical operation, Micro-computed tomographic results indicated a significant reduction in t the size of the rat skull defect. The red area shown in Fig. 7A,B represent the initial defect location and size (Fig. 7A,B). Compared to the blank group, the HAMT-CHS groups showed significantly different BS, Tb.N, BS/TV, and BV/TV values, while Tb.Th, Tb.Sp, and BS/BV showed no significant difference (*p*-value < 0.05) (Fig. 7C). H&E and Masson staining of histological sections showed obvious new bone at the junction of the scaffold and defect, indicating that there were active osteoblasts at the edge of bone defect. Scaffolds provide a framework for initial bone formation, and are conducive to the adhe-sion, proliferation and differentiation of osteoblasts. On the other hand, more vascular tissues could be observed in the scaffolds group, indicating the pore structure was conducive to the growth of blood vessels and could provide a sufficient blood supply for osteogenic differentiation (Fig. 7D). These observations, demonstrate good biocompatibility of the HAMT-CHS scaffold.

4. Discussion

The scaffold composition and the chemical composition of its surface determine its ability to attach cells. The scaffold structure plays a key role in controlling the ability of cells to migrate. The ideal scaffold structure is conducive to cell penetration. Moreover, it also allows nutrients and oxygen to flow into the scaffold, and waste products produced by the cells to flow out, thus improving cell survival. The design of scaffolds must therefore include sufficient porosity, which need to be large enough to allow the dis-
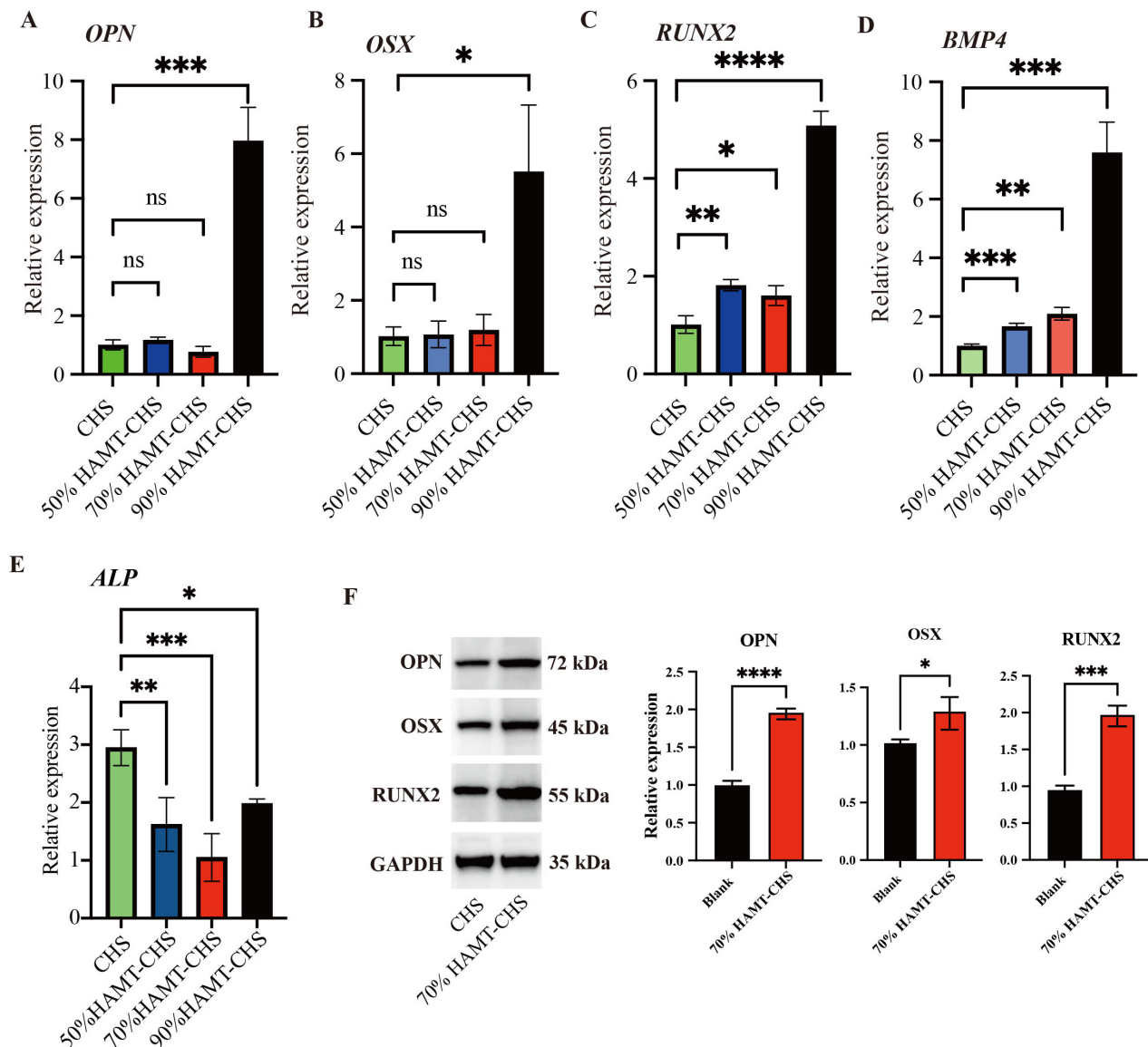
Fig. 5. RT-PCR and WB results for selected genes. (A–E) RT-PCR results of gene *OPN* (A), *OSX* (B), *RUNX2* (C), *BMP4* (D), and *ALP* (E) (Sample size n = 4). (F) The protein expression level of the three proteins, right panel was the quantitative results (Sample size n = 3). "*", "**", "***", "****" represent $p < 0.05$, $p < 0.01$, $p < 0.001$, $p < 0.0001$, respectively; ns represents non-significant. WB, Western blot; OPN, osteopontin; OSX, Osterix; RUNX2, runt-related transcription factor 2; GAPDH, glyceraldehyde-3-phosphate dehydrogenase; RT-PCR, quantitative real-time polymerase chain reaction.

tribution of cells. Many researchers have investigated the effect of void size on bone regeneration [22,23]. Kuboki *et al*. [24] reported that the optimal osteogenic pore size of porous HAP blocks was 300–400 μm.

Smaller diameter pores (90–120 μm) in straight tunnel structures of different diameters in honeycombed HAP can induce cartilage formation and then bone formation, while larger diameter tunnels (350 μm) induce bone formation directly within the tunnel [24]. Zhang *et al*. [25] reported that the pore size of 150–250 μm in a collagen porous gradient scaffold provides a more favorable three-dimensional microenvironment for cartilage matrix expression and cartilage differentiation. Moreover, small pores are more easily

filled with proliferating cells, thus increasing the interaction between cells [25]. Oh *et al*. [26] synthesized polyacetate gradient pore size scaffolds by centrifugation, and found great differences in the growth of cells and tissues according to the pore size of the scaffolds. Chondrocytes and osteoblasts grow well with a pore size of 380–405 μm, fibroblasts in a pore size of 186–200 μm, while a pore size of 290–310 μm was more suitable for bone formation [26]. Griffon *et al*. [27] found that chondrocyte proliferation and metabolic activities were more active in chitosan scaffolds with a pore size of 70–120 μm. Li *et al*. [28] prepared HAP scaffolds with three different large pore sizes of 500–650 μm, 750–900 μm, and 1100–1250 μm. The rates of an-
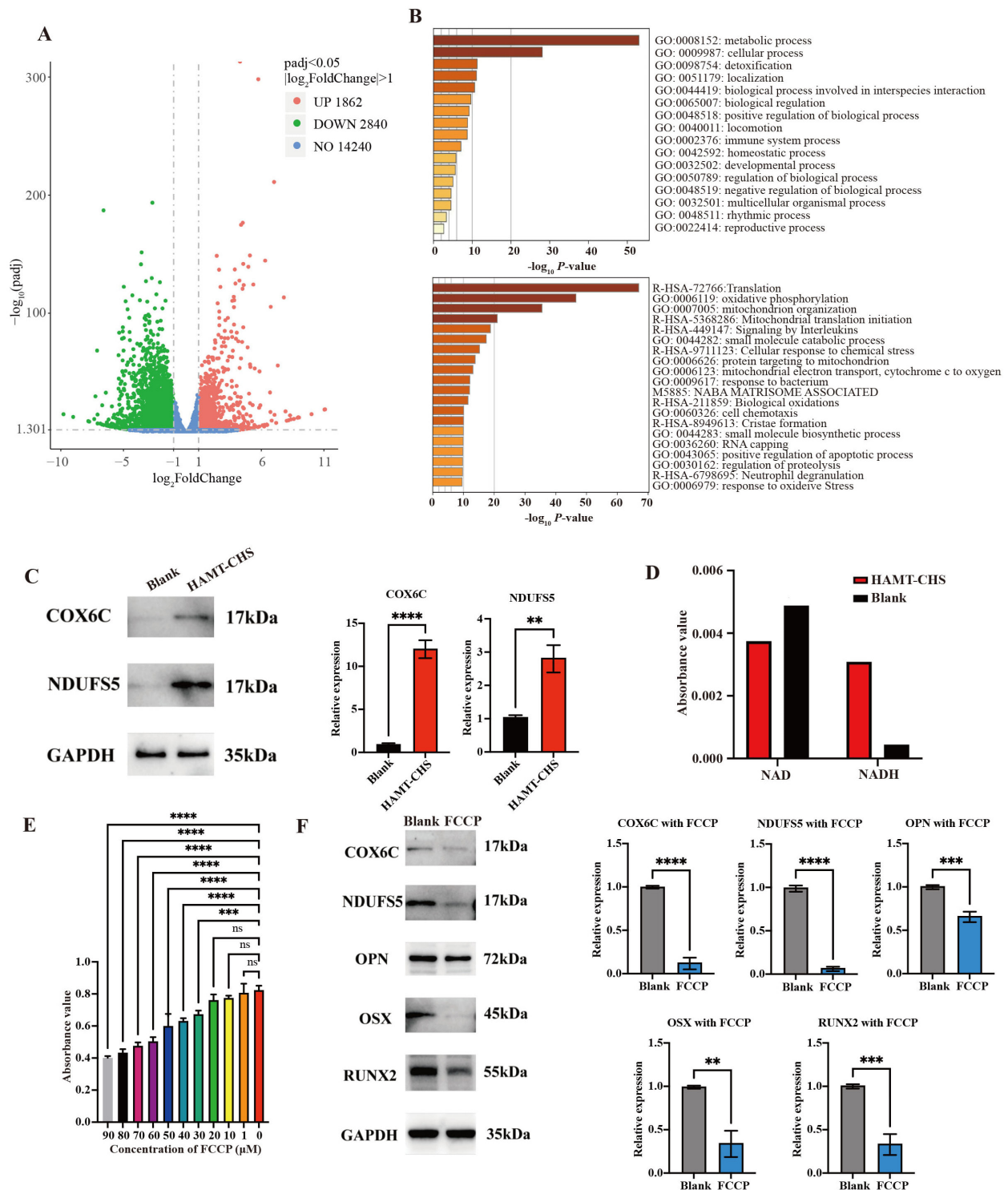
Fig. 6. HAMT-CHS activated the oxidative phosphorylation pathway of BMSCs. (A) Volcano plot showing the number of DEGs. (B) GO (top) and KEGG (bottom) enrichment analysis results for up-regulated DEGs. (C) WB results showing the expression levels of oxidative phosphorylation related proteins COX6C and NDUFS5; right panel was the quantitative results (Sample size n = 3). (D) Detection of the expression of NAD/NADH content in BMSCs. (E) CCK-8 assay results to predict cell proliferation level affected by FCCP (Sample size n = 4). (F) WB results showing the expression levels of osteogenic differentiation related proteins (Sample size n = 3); right panel was the quantitative results. "**", "***", "****" represent $p < 0.01$, $p < 0.001$, $p < 0.0001$, respectively; ns represents non-significant. DEGs, differentially expressed genes; GO, Gene ontology; KEGG, Kyoto Encyclopedia of Genes and Genomes; COX6C, cytochrome c oxidase subunit 6c; NDUFS5, Fe-S protein 5; FCCP, carbonyl cyanide 4-(trifluoromethoxy) phenylhydrazone; NAD, Nicotinamide adenine dinucleotide; NADH, nicotinamide-adenine dinucleotide.
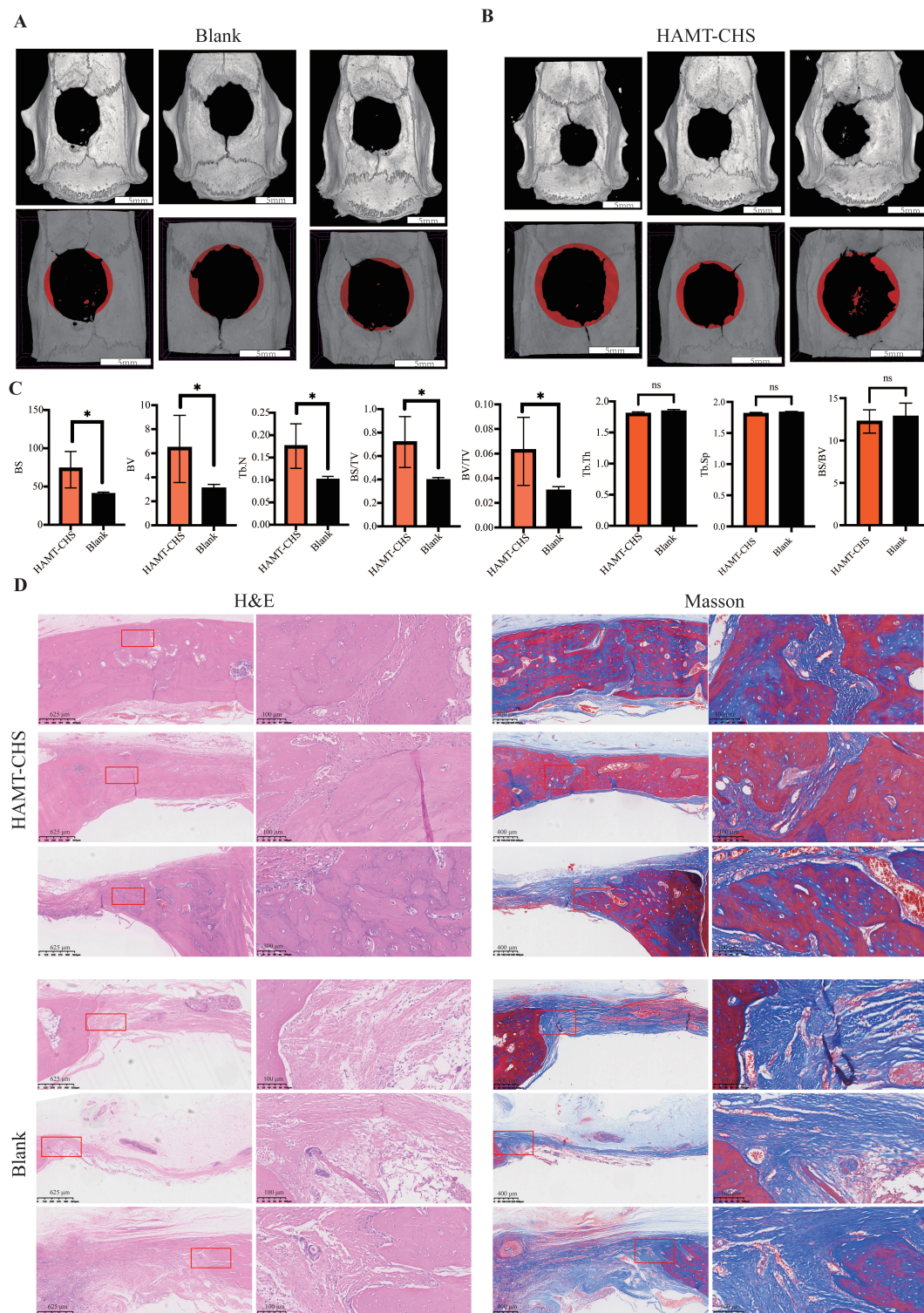
Fig. 7. Animal experiment validated the biocompatibility of HAMT-CHS. (A,B) Micro-CT images. The red part marks the new bone. Scale bar: 5 mm. (C) Bone tissue related evaluation indicators: BS, BV, Tb.N, BS/TV, BV/TV, Tb.Th, Tb.Sp, and BS/BV; "*" represents $p < 0.05$, ns represents non-significant. (D) H&E and Masson staining of histological sections showed that the new bone was obvious at the junction of scaffold and defect, indicating that there were active osteoblasts at the edge of bone defect (Sample size n = 3) (a–c, g-i Scale bar: 625 µm; d–f, j–l Scale bar: 100 µm; m–o, s–u Scale bar: 400 µm; p–r, v–x Scale bar: 100 µm). CT, computed tomographic; BS, bone surface; BV, bone volume; Tb.N, trabecular number; BS/TV, bone surface area density; BV/TV, bone volume fraction; Tb.Th, trabecular thickness; Tb.Sp, trabecular separation; BS/BV, bone surface fraction.

giogenesis and osteogenesis observed in the 750–900 µm large-aperture scaffolds were significantly faster than those of the other two large-aperture scaffolds, and the new bone was evenly distributed. These results demonstrate the importance of appropriately large apertures in HAP scaffolds with similar interconnect structures, thereby providing an environment for heterotopic osteogenesis and angiogenesis [28]. Furthermore, the pores need to be connected to each other to allow cells to migrate between them. In general, cells distribute easily in the peripheral area of the scaffold, resulting in tissue regeneration only in the outermost layer. For successful tissue engineering, a uniform distribution of cells throughout the scaffold is required [29]. Amini and Nukavarapu [30] speculated that insufficient vascularization inside the scaffold would lead to insufficient oxygen tension and a lack of nutrient supply, leading to cell death and thus affecting bone formation. By optimizing the pore distribution and porosity, the survival of cells in the scaffold could be improved and hence the formation of new bone increased [30]. Interconnected pores increase the ability of cells to proliferate, and speed up the flow of nutrients and elimination of waste. Moreover, the rate of material degradation was found to be inversely proportional to the porosity [31]. Porosity is a very important issue, and refers to the remaining spatial proportion of scaffolds with tissue growth during the process of bone defect repair. This has a major influence on the proliferation of osteoblasts and on the ability to induce bone formation. Safari *et al*. [32] reported that the porosity of human bone ranges from 30% to 90%, and argued that the porosity of effective bone tissue regeneration scaffolds should be >60–90%. The optimal range of porosity has yet to be determined. Increased porosity will inevitably reduce the strength of the scaffold, but it should be >50%–60% [33]. Sanzana *et al*. [34] implanted two scaffolds with different porosity into New Zealand rabbits to compare their osteogenic effect. The high porosity scaffolds (82%) were found have significantly better osteogenic ability than low porosity scaffolds (37%) [34].

The cells in scaffolds with uniform pores are more fluid, and thus more likely to flow through the scaffolds, thereby reducing the opportunity to react with the scaffold materials. The internal structure of natural bone tissue is not uniform, and the porous bone cancellous structure formed by the internal bone trabeculae gradually transitions to a dense bone structure with a dense surface. The osteogenic effect of scaffolds with gradient pore structure is better than that of scaffolds with uniform pore structure [35]. Sobral *et al*. [36] inoculated a gradient pore scaffold and a uniform pore scaffold with an equal number of cells. The gradient pore scaffold showed a higher rate of cell inoculation, and a more uniform distribution of cells, as observed by fluorescent staining [36]. A rough scaffold surface is more conducive to cell attachment and proliferation than a smooth surface. Wang *et al*. [37] found that a rough surface provides better anchoring for the filamentous foot. Calore *et al*. [38] inoculated cells on two different scaffolds and cultured

them for 7 days to evaluate the expression of osteogenic genes. The expression of ALP in the scaffolds with rough surfaces and micropores was significantly higher than in PLLA scaffolds with smooth surfaces [38]. Gaharwar *et al*. [39] added nanoclays to electrospun polycaprolactone scaffolds to form rough surfaces. The roughness of these scaffolds was due to the diameter of the fibers and to the uneven distribution of nanoclays within the fibers. The cells can easily fill the substrate by anchoring and stretching over the microsized rough structure, resulting in increased metabolic activity of the adherent cells [39]. The bone formation seen after 12 weeks in of polypropylene glycol fumarate composite scaffold with ultra-short single-wall carbon nanotubes was 3-fold higher than the control scaffold. Furthermore, the porosity, surface roughness and chemical properties of the original scaffold were improved by carbon nanotubes [40].

Review of the literature reveals much discussion of, scaffold design, but there is no consensus on the most suitable factors for osteogenesis with regard pore size, porosity and surface roughness. It is generally believed that scaffolds with pores >300 µm are suitable for osteogenesis. In addition, the pore scaffolds need to be interconnected, which is conducive to the entry of nutrients and oxygen and the elimination of waste. Therefore, wax balls of controlled diameter were prepared with an emulsification method as pore-making agent, allowing the synthesis of scaffolds-with internal pores of 300–500 µm and peripheral pores of 1000 µm. The scaffolds-with gradient distribution from the inside to the outside, and the pores were interconnected. The porosity was 88.8% > 60%, and therefore constituting a high porosity scaffold. SEM of the scaffold microstructure revealed a rough internal surface which was conducive to cell attachment. The compressive strength of natural bone varies between cortical bone (100–200 MPa) and cancellous bone (2–20 MPa) [41]. The large difference in stiffness of implant materials and natural bone can easily lead to a "stress shielding" effect and bone resorption [42]. In the present study, the elastic modulus of 70% HAMT-CHS was 166.717 ± 0.031 MPa. This is close to the compressive strength of cortical bone and therefore it can provide some support in the early stage of bone regeneration.

The differentially expressed genes were identified by RNA-seq, KEGG and GO analysis subsequently showed that oxidative phosphorylation was significantly up-regulated in these scaffolds. The process of combining hydrogen atoms obtained from the metabolism of materials with oxygen to form water through the electron transport chain gradually releases energy that is stored in ATP. The oxidation of hydrogen and the phosphorylation of ADP are coupled during oxidative phosphorylation. During this process, hydrogen removed by intermediate metabolites is transferred by a series of enzymes or coenzymes, and is finally combined with oxygen to form water. This series of enzymes and coenzymes are referred to as hydrogen and electron carriers. They are arranged in a spe-

cific order on the inner membrane of the mitochondria to form the electron transport chain, also known as the respiratory chain. Hydrogen carriers or electron carriers have redox properties, and can transfer oxygen atoms and electrons. The hydrogen and electron transmitter components of the electron transport chain mostly belong to one of the following five categories: (1) Nicotinamide adenine dinucleotide (NAD+) or coenzyme I; (2) One of the many kinds of flavin proteins, or flavin mononucleotide (FMN) and flavin adenine dinucleotide (FAD) cogroups; (3) Ferrothionein; (4) Ubiquinone; (5) Cytochrome (Cyt). One of the two electron transport chains in the body, starts with NADH and the other one starts with FAD. Inhibitors of oxidative phosphorylation fall into two broad categories. The one category is electron transport chain inhibitors, such as rotenone, which block the transfer of electrons from NADH to ubiquinone; Antimycin A and dimercaptopropanol inhibit electron transfer from Cytb to Cytc. The other category is the uncoupling agents, that separate oxidation form phosphorylation so that ATP can no longer be produced [43].

NDUFS5 is a member of the NADH dehydrogenase (ubiquinone) iron-sulfur protein family. The encoded protein is a subunit of NADH: ubiquinone oxidoreductase (complex I). This is the first enzyme complex in the electron transport chain and is located on the inner mitochondrial membrane. COX6C, the terminal enzyme of the mitochondrial respiratory chain, catalyzes the electron transfer from reduced Cyt c to oxygen. It is a heteromeric complex consisting of three catalytic subunits encoded by mitochondrial genes, as well several structural subunits encoded by nuclear genes. The function of the mitochondrially-encoded subunits is electron transfer, while the nuclear-encoded subunits may be involved in the regulation and assembly of the complex. Therefore, the up-regulation of NDUFS5 and COX6C protein expression confirms activation of the oxidative phosphorylation pathway [43]. FCCP is a potent uncoupling agent for oxidative phosphorylation in mitochondria, thereby inhibiting the synthesis of ATP by transporting protons. In the present study, the expression of NDUFS5, COX6C, RUNX2, OPN, and OSX was examined following FCCP treatment. The expression levels were significantly lower, indicating that oxidative phosphorylation was inhibited and osteogenesis was reduced. Lee et al. [44] reported that osteoblast-mediated bone formation is usually powered by oxidative phosphorylation and glycolysis, both of which produce ATP. Safari et al. [45] found that phosphorylated proteins present in the extracellular matrix play a crucial role in regulating the mineralization process. Phosphorylated scaffolds provide new nucleation sites for mineral deposition within their collagen fibers. Recapitulating the function of natural phosphoproteins is an effective way to increase apatite formation [45]. Oxidative phosphorylation is also a major metabolic pathway for meeting the energy requirements of osteoclasts [46]. The mechanism underlying the effect of the scaffold on the expression levels of genes in oxidative phosphorylation is still unclear and requires further investigation.

5. Conclusion

The HAMT-CHS gradient pore scaffold has good biocompatibility, excellent porosity and a reasonable gradient pore structure. The results of both in vivo and in vitro experiments demonstrate that HAMT-CHS has good osteogenic properties. High-throughput sequencing helped to understand the mechanism of osteogenesis induced by this scaffold. The previous study has also demonstrated that oxidative phosphorylation plays an important role in bone formation [43]. However, the mechanism by which scaffolds induce oxidative phosphorylation requires further study. In view of the good drug loading and slow-release ability of HAMT, osteogenic induction factors could also be loaded onto the scaffold at a later stage. Wax ball perforation technology can impact the biocompatibility of scaffold, and 3D printing technology also has the potential for further development. 3D printing has made it possible to directly combine materials, cells and growth factors to produce regenerative materials [47]. In the future, it may be possible find substances in natural foods that are similar to growth factors and can be loaded onto tissue engineering scaffolds to enhance the osteogenic induction effect [48]. This study provides practical experience in the design of biological scaffolds that should help to accelerate their clinical application in future.

Availability of Data and Materials

The data sets generated and/or analyzed during the current study are not publicly available due to some of the data may be used for future research but are available from the corresponding author on reasonable request.

Author Contributions

LSL: Ideas, Supervision. ZLZ: Performing the experiments, and data/evidence collection, writing the initial draft. WS: Methodology, Software. Both authors contributed to editorial changes in the manuscript. Both authors read and approved the final manuscript. Both authors have participated sufficiently in the work and agreed to be accountable for all aspects of the work.

Ethics Approval and Consent to Participate

All procedures followed were in accordance with the ethical standards of the responsible committee on 'Animal Research: Reporting In Vivo Experiments' (ARRIVE) 2.0 guidelines. The study was reviewed and approved by the Ethics Committee of Changzhi medical College, with approval No: DW2022082.

Acknowledgment

Funding

Conflict of Interest

The authors declare no conflict of interest.

References

[1] Feng Long, Hailong Li, Xujun Chen, Yiqun He, Youhai Dong. Exosomal miR-423-5p Derived from Mineralized Osteoblasts Promotes Angiogenesis of Endothelial Cells by Targeting CXCL10. Frontiers in Bioscience (Landmark edition). 2024; 29: 278. https://doi.org/10.31083/j.fbl2908278.

[2] Koushik TM, Miller CM, Antunes E. Bone Tissue Engineering Scaffolds: Function of Multi-Material Hierarchically Structured Scaffolds. Advanced Healthcare Materials. 2023; 12: e2202766. https://doi.org/10.1002/adhm.202202766.

[3] Arcos D, Vallet-Regí M. Substituted hydroxyapatite coatings of bone implants. Journal of Materials Chemistry. B. 2020; 8: 1781–1800. https://doi.org/10.1039/c9tb02710f.

[4] Ma H, Xue L, Nie T. Fabrication of PLLA scaffold with gradient macro/micro/nano structure by electrophoretic deposition of carbon nanotube. Materials Letters. 2015; 159: 185–188. https://doi.org/10.1016/j.matlet.2015.06.088.

[5] Kolos EC, Ruys AJ, Rohanizadeh R, Muir MM, Roger G. Calcium phosphate fibres synthesized from a simulated body fluid. Journal of Materials Science. Materials in Medicine. 2006; 17: 1179–1189. https://doi.org/10.1007/s10856-006-0546-3.

[6] Kolos EC, Ruys AJ. Osteoblast attachment to hydroxyapatite micro-tube scaffolds. Journal of Materials Science. Materials in Medicine. 2014; 25: 1801–1817. https://doi.org/10.1007/s10856-014-5212-6.

[7] Hui J, Xiang G, Xu X, Zhuang J, Wang X. Monodisperse F-substituted hydroxyapatite single-crystal nanotubes with amphiphilic surface properties. Inorganic Chemistry. 2009; 48: 5614–5616. https://doi.org/10.1021/ic900697b.

[8] Chandanshive BB, Rai P, Rossi AL, Ersen O, Khushalani D. Synthesis of hydroxyapatite nanotubes for biomedical applications. Materials Science & Engineering. C, Materials for Biological Applications. 2013; 33: 2981–2986. https://doi.org/10.1016/j.msec.2013.03.022.

[9] Zhang YG, Zhu YJ, Chen F, Sun TW, Jiang YY. Ultralong hydroxyapatite microtubes: solvothermal synthesis and application in drug loading and sustained drug release. CrystEngComm. 2017; 19: 1965–1973. https://doi.org/10.1039/C6CE02394K.

[10] Iijima S. Helical microtubes of graphitic carbon. Nature. 1991; 354: 56–58. https://doi.org/10.1038/354056a0.

[11] Kostarelos K. The long and short of carbon nanotube toxicity. Nature Biotechnology. 2008; 26: 774–776. https://doi.org/10.1038/nbt0708-774.

[12] Yuan Y, Liu C, Zhang Y, Shan X. Sol–gel auto-combustion synthesis of hydroxyapatite nanotubes array in porous alumina template. Materials Chemistry & Physics. 2008; 112: 275–280. https://doi.org/10.1016/j.matchemphys.2008.05.068.

[13] Ma MG, Zhu YJ, Chang J. Solvothermal preparation of hydroxyapatite microtubes in water/N,N-dimethylformamide mixed solvents. Materials Letters. 2008; 62: 1642–1645. https://doi.org/10.1016/j.matlet.2007.09.050.

[14] Dozzo A, Chullipalliyalil K, McAuliffe M, O'Driscoll CM, Ryan KB. Nano-Hydroxyapatite/PLGA Mixed Scaffolds as a Tool for Drug Development and to Study Metastatic Prostate Cancer in the Bone. Pharmaceutics. 2023; 15: 242. https://doi.org/10.3390/pharmaceutics15010242.

[15] Liang H, Wang Y, Chen S, Liu Y, Liu Z, Bai J. Nano-Hydroxyapatite Bone Scaffolds with Different Porous Structures Processed by Digital Light Processing 3D Printing. International Journal of Bioprinting. 2022; 8: 502. https://doi.org/10.18063/ijb.v8i1.502.

[16] Zhang YG, Zhu YJ, Chen F, Sun TW. Biocompatible, Ultralight, Strong Hydroxyapatite Networks Based on Hydroxyapatite Microtubes with Excellent Permeability and Ultralow Thermal Conductivity. ACS Applied Materials & Interfaces. 2017; 9: 7918–7928. https://doi.org/10.1021/acsami.6b13328.

[17] Zhang YG, Zhu YJ, Chen F, Sun TW. A novel composite scaffold comprising ultralong hydroxyapatite microtubes and chitosan: preparation and application in drug delivery. Journal of Materials Chemistry. B. 2017; 5: 3898–3906. https://doi.org/10.1039/c6tb02576e.

[18] Zhang YG, Zhu YJ, Chen F, Lu BQ. Dopamine-modified highly porous hydroxyapatite microtube networks with efficient near-infrared photothermal effect, enhanced protein adsorption and mineralization performance. Colloids and Surfaces. B, Biointerfaces. 2017; 159: 337–348. https://doi.org/10.1016/j.colsurfb.2017.07.093.

[19] Zeng Q, Li K, Fen-Chong T, Dangla P. Pore structure characterization of cement pastes blended with high-volume fly-ash. Cement & Concrete Research. 2012; 42: 194–204. https://doi.org/10.1016/j.cemconres.2011.09.012.

[20] Love MI, Huber W, Anders S. Moderated estimation of fold change and dispersion for RNA-seq data with DESeq2. Genome Biology. 2014; 15: 550. https://doi.org/10.1186/s13059-014-0550-8.

[21] Xiao W, Wang RS, Handy DE, Loscalzo J. NAD(H) and NADP(H) Redox Couples and Cellular Energy Metabolism. Antioxidants & Redox Signaling. 2018; 28: 251–272. https://doi.org/10.1089/ars.2017.7216.

[22] Jin HH, Kim DH, Kim TW, Shin KK, Jung JS, Park HC, *et al*. In vivo evaluation of porous hydroxyapatite/chitosan-alginate composite scaffolds for bone tissue engineering. International Journal of Biological Macromolecules. 2012; 51: 1079–1085. https://doi.org/10.1016/j.ijbiomac.2012.08.027.

[23] Dai C, Li Y, Pan W, Wang G, Huang R, Bu Y, *et al*. Three-Dimensional High-Porosity Chitosan/Honeycomb Porous Carbon/Hydroxyapatite Scaffold with Enhanced Osteoinductivity for Bone Regeneration. ACS Biomaterials Science & Engineering. 2020; 6: 575–586. https://doi.org/10.1021/acsbiomaterials.9b01381.

[24] Kuboki Y, Jin Q, Takita H. Geometry of carriers controlling phenotypic expression in BMP-induced osteogenesis and chondrogenesis. The Journal of Bone and Joint Surgery. American Volume. 2001; 83-A: S105–S115.

[25] Zhang Q, Lu H, Kawazoe N, Chen G. Preparation of collagen porous scaffolds with a gradient pore size structure using ice particulates. Materials Letters. 2013; 107: 280–283. https://doi.org/10.1016/j.matlet.2013.05.070.

[26] Oh SH, Park IK, Kim JM, Lee JH. In vitro and in vivo characteristics of PCL scaffolds with pore size gradient fabricated by a centrifugation method. Biomaterials. 2007; 28: 1664–1671. https://doi.org/10.1016/j.biomaterials.2006.11.024.

[27] Griffon DJ, Sedighi MR, Schaeffer DV, Eurell JA, Johnson AL. Chitosan scaffolds: interconnective pore size and cartilage engineering. Acta Biomaterialia. 2006; 2: 313–320. https://doi.org/10.1016/j.actbio.2005.12.007.

[28] Li J, Zhi W, Xu T, Shi F, Duan K, Wang J, *et al*. Ectopic osteogenesis and angiogenesis regulated by porous architecture of hydroxyapatite scaffolds with similar interconnecting structure in vivo. Regenerative Biomaterials. 2016; 3: 285–297. https://doi.org/10.1093/rb/rbw031.

[29] Chen G, Kawazoe N. Porous Scaffolds for Regeneration of Cartilage, Bone and Osteochondral Tissue. Advances in Experimental Medicine and Biology. 2018; 1058: 171–191. https://doi.org/10.1007/978-3-319-76711-6_8.

[30] Amini AR, Nukavarapu SP. Oxygen-tension controlled matrices for enhanced osteogenic cell survival and performance. Annals of Biomedical Engineering. 2014; 42: 1261–1270. https://doi.org/10.1007/s10439-014-0990-z.

[31] van Tienen TG, Heijkants RGJC, Buma P, de Groot JH, Pennings AJ, Veth RPH. Tissue ingrowth and degradation of two biodegradable porous polymers with different porosities and pore sizes. Biomaterials. 2002; 23: 1731–1738. https://doi.org/10.1016/s0142-9612(01)00280-0.

[32] Safari B, Aghanejad A. Porous gelatin-based phosphorylated scaffold: Microstructure, cell response and osteogenic differentiation of human adipose-derived mesenchymal stem cells. Journal of Drug Delivery Science and Technology. 2024; 99: 106008. https://doi.org/10.1016/j.jddst.2024.106008.

[33] Perez RA, Mestres G. Role of pore size and morphology in musculo-skeletal tissue regeneration. Materials Science & Engineering. C, Materials for Biological Applications. 2016; 61: 922–939. https://doi.org/10.1016/j.msec.2015.12.087.

[34] Sanzana ES, Navarro M, Ginebra MP, Planell JA, Ojeda AC, Montecinos HA. Role of porosity and pore architecture in the in vivo bone regeneration capacity of biodegradable glass scaffolds. Journal of Biomedical Materials Research. Part a. 2014; 102: 1767–1773. https://doi.org/10.1002/jbm.a.34845.

[35] Chen H, Liu Y, Wang C, Zhang A, Chen B, Han Q, et al. Design and properties of biomimetic irregular scaffolds for bone tissue engineering. Computers in Biology and Medicine. 2021; 130: 104241. https://doi.org/10.1016/j.compbiomed.2021.104241.

[36] Sobral JM, Caridade SG, Sousa RA, Mano JF, Reis RL. Three-dimensional plotted scaffolds with controlled pore size gradients: Effect of scaffold geometry on mechanical performance and cell seeding efficiency. Acta Biomaterialia. 2011; 7: 1009–1018. https://doi.org/10.1016/j.actbio.2010.11.003.

[37] Wang YW, Wu Q, Chen GQ. Attachment, proliferation and differentiation of osteoblasts on random biopolyester poly(3-hydroxybutyrate-co-3-hydroxyhexanoate) scaffolds. Biomaterials. 2004; 25: 669–675. https://doi.org/10.1016/s0142-9612(03)00561-1.

[38] Calore AR, Srinivas V, Groenendijk L, Serafim A, Stancu IC, Wilbers A, et al. Manufacturing of scaffolds with interconnected internal open porosity and surface roughness. Acta Biomaterialia. 2023; 156: 158–176. https://doi.org/10.1016/j.actbio.2022.07.017.

[39] Gaharwar AK, Mukundan S, Karaca E, Dolatshahi-Pirouz A, Patel A, Rangarajan K, et al. Nanoclay-enriched poly(ε-caprolactone) electrospun scaffolds for osteogenic differentiation of human mesenchymal stem cells. Tissue Engineering. Part a. 2014; 20: 2088–2101. https://doi.org/10.1089/ten.tea.2013.0281.

[40] Sitharaman B, Shi X, Walboomers XF, Liao H, Cuijpers V, Wilson LJ, et al. In vivo biocompatibility of ultra-short single-walled carbon nanotube/biodegradable polymer nanocomposites for bone tissue engineering. Bone. 2008; 43: 362–370. https://doi.org/10.1016/j.bone.2008.04.013.

[41] Vesvoranan O, Anup A, Hixon KR. Current Concepts and Methods in Tissue Interface Scaffold Fabrication. Biomimetics. 2022; 7: 151. https://doi.org/10.3390/biomimetics7040151.

[42] Chmielewska A, Dean D. The role of stiffness-matching in avoiding stress shielding-induced bone loss and stress concentration-induced skeletal reconstruction device failure. Acta Biomaterialia. 2024; 173: 51–65. https://doi.org/10.1016/j.actbio.2023.11.011.

[43] Wilson DF. Oxidative phosphorylation: regulation and role in cellular and tissue metabolism. The Journal of Physiology. 2017; 595: 7023–7038. https://doi.org/10.1113/JP273839.

[44] Lee WC, Guntur AR, Long F, Rosen CJ. Energy Metabolism of the Osteoblast: Implications for Osteoporosis. Endocrine Reviews. 2017; 38: 255–266. https://doi.org/10.1210/er.2017-00064.

[45] Safari B, Aghanejad A, Kadkhoda J, Aghazade M, Roshangar L, Davaran S. Biofunctional phosphorylated magnetic scaffold for bone tissue engineering. Colloids and Surfaces. B, Biointerfaces. 2022; 211: 112284. https://doi.org/10.1016/j.colsurfb.2021.112284.

[46] Park-Min KH. Metabolic reprogramming in osteoclasts. Seminars in Immunopathology. 2019; 41: 565–572. https://doi.org/10.1007/s00281-019-00757-0.

[47] Salahshour P, Abdolmaleki S, Monemizadeh S, Gholizadeh S, Khaksar S. Nanobiomaterials/Bioinks Based Scaffolds in 3d Bioprinting for Tissue Engineering and Artificial Human Organs. Advances in Biology & Earth Sciences. 2024; 9: 97–104. https://doi.org/10.62476/abes9s97.

[48] Karadağ M, Omarova S. USE OF Prunus armeniaca L. Seed oil and pulp in health and cosmetic products. Advances in Biology & Earth Sciences. 2024; 9: 105–110. https://doi.org/10.62476/abess105.